Soft Matter

PAPER

View Article Online
View Journal | View Issue

Open Access Article. Published on 17 August 2020. Downloaded on 12/4/2025 7:16:20 PM.
This article is licensed under a Creative Commons Attribution 3.0 Unported Licence.

Check for updates

Cite this: *Soft Matter*, 2020, **16**, 8453

Colloidal assembly of polydisperse particle blends during drying†

Yichen Dong,[a] Nicolas Busatto,[b] Peter J. Roth[b] and Ignacio Martin-Fabiani*[a]

Received 30th April 2020,
Accepted 11th August 2020

DOI: 10.1039/d0sm00785d

rsc.li/soft-matter-journal

In this work, we synthesize a polydisperse aqueous colloidal system composed of small and large zwitterionic particles, as well as medium sized standard acrylic particles. By assembling these dispersions into films by drying, we show using atomic force microscopy (AFM) how their top surfaces can be mostly covered by zwitterionic groups for a wide range of evaporation rates. We probe underneath the top film surface using Fourier-transform infrared (FTIR) spectroscopy – attenuated total reflection (ATR), observing that the content in zwitterionic particles of the film upper layer increases for faster evaporation rates. We show how polydisperse systems hold great potential to overcome the evaporation rate dependence of size segregation processes in drying colloidal blends, and we provide further insights into the assembly mechanisms involved. Polydisperse blends enhance the robustness of such processes for application in coatings and other soft products where evaporation rate can not be tuned.

Introduction

Polymer particles dispersed in water, forming what is known as a latex dispersion, have a key role in the formulation of products such as inks,[1,2] paints,[3–5] coatings[6,7] or adhesives.[8] After one of the aforementioned products is applied on a surface, the latex film formation process begins. Water starts evaporating and particles diffuse away from the receding air–water interface. If the water evaporation rate is faster than the diffusion of particles, they will get trapped at the air–water interface.[9] This phenomenon had been seen as a negative effect until a few years ago, as it was linked to the formation of a skin layer of coalesced particles at the top of the drying film which prevents the evaporation of water from the bulk.[10]

A few years ago, Fortini *et al.* showed in experiments and modelling that such a vertical concentration gradient can be harnessed in drying bimodal blends to fabricate stratified films with mainly small particles at the top and mainly large particles at the bottom.[11] Later on, they expanded the concept by carrying out modelling of drying ternary and polydisperse blends.[12] Experimentally, a recent study on lignin particles has demonstrated the size segregation that takes place during drying in polydisperse colloidal systems.[13] A surge of works in this area has proven that the extent and effectiveness of the stratification process is strongly dependent on a number of parameters, including: particle size ratio,[11,14] evaporation rate,[11,14] volume fraction,[15,16] and temperature gradients.[17] Molecular dynamics studies, comparing simulations carried out using implicit and explicit solvent, have proven that hydrodynamic interactions must be considered to paint a more complete picture of the process.[18,19] It seems clear now that stratification is a complex phenomenon whose effectiveness depends on a large amount of internal and external factors. Such sensitivity limits its reliability to be harnessed in actual industrial products. For this reason, in this study we have designed a polymer particle system that overcomes some of those limitations and harness size segregation to obtain the desired film surface for a wide range of evaporation rates and compositions.

We designed a colloidal system to harness size segregation in drying particle blends and enrich the film surface with zwitterionic groups. Zwitterionic polymers contain oppositely charged cationic and anionic groups in every repeat unit,[20] the most common groups being sulfobetaines (SB), carboxybetaines (CB), and phosphorylcholines (PC).[20,21] In the case of betaines, thanks to their anti-polyelectrolyte and low protein fouling behaviour as well as their biocompatibility, they find application as emulsifiers,[22] biosensors,[23,24] separation membranes,[25] and marine coatings.[26] There have been several successful attempts to synthesize discrete polybetaine particles involving the sulfobetaine poly(3-dimethyl(methacryloyloxyethyl)ammonium propane sulfonate) (pDMAPS). To the best of our knowledge, these studies focus on the production of gel particles[27] or heavily cross-linked particles[28,29] which are either too soft or unlikely to form a film. Gui *et al.* used layer-by-layer self-assembly to fabricate bulk PDMAPS/poly(acrylic acid) (PAA) multilayer films with controllable disintegration.[30] Therefore, there is a gap in the

[a] *Department of Materials, Loughborough University, Loughborough, Leicestershire LE11 3TU, UK. E-mail: i.martin-fabiani@lboro.ac.uk*
[b] *Department of Chemistry, University of Surrey, Guildford, Surrey, GU2 7XH, UK*

† Electronic supplementary information (ESI) available: ^{1}H NMR spectra of purified pDMAPS and pDMAPs-*block-stat*-pEHMA; heat flow *vs.* T for zwitterionic particles; roughness of film surfaces; FTIR-ATR scans across diagonals of dried films; AFM topography maps of only zwitterionic particle films. See DOI: 10.1039/d0sm00785d

Open Access Article. Published on 17 August 2020. Downloaded on 12/4/2025 7:16:20 PM.
This article is licensed under a Creative Commons Attribution 3.0 Unported Licence.

literature for the synthesis of PDMAPS-containing particles with good film forming properties for colloidal coatings applications.

Here, we designed a polydisperse colloidal system by blending acrylic polymer particles in water and newly synthesized polymer particles with a zwitterionic PDMAPS shell. The size distribution and composition of this system was tailored in order to minimize the influence of evaporation rate on the final film surface composition after drying. Our work provides valuable insights on how to enhance the reliability of size segregation in drying particle blends for applications where the water evaporation rate cannot be tuned. This includes not only paints and coatings, but also in other soft products such as inks or adhesives.

Experimental

Materials

[2-(Methacryloyloxy)ethyl]dimethyl-(3-sulfopropyl)ammonium hydroxide (DMAPS, Sigma Aldrich), 4-cyanopentanoic acid dithiobenzoate (CPADB, Sigma Aldrich), and 2,2,2-trifluoroethanol (TFE, Sigma Aldrich) were used as received. 2,2-Azobisisobutyronitrile (AIBN, Sigma Aldrich). AIBN was recrystallized from methanol and stored in a freezer. *n*-Butyl methacrylate (*n*BuMA, Alpha Aesar) and 2-ethylhexyl methacrylate (EHMA, Alpha Aesar) were passed through a column of basic aluminium oxide to remove inhibitors. The monomers methyl methacrylate (MMA, purity 99.9%, 45–55 ppm monomethyl ether hydroquinone (MEHQ), Quimidroga), *n*-butyl acrylate (BA, purity 99.5%, 10–20 ppm MEHQ, Quimidroga) and sodium *p*-styrene sulfonate (NaSS, purity ≥90%, Sigma Aldrich), the components of the redox initiator system (oxidant *tert*-butyl hydroperoxide, TBHP, 70 wt% aqueous solution, Luperox, Sigma Aldrich, and reductant ascorbic acid, AsAc, purity ≥99%, Acros), and the conventional surfactant sodium dodecyl sulfate (SDS, Sigma-Aldrich) were used without further purification. Distilled water was utilized in all the reactions. Hydroquinone (HQ, purity 99%, Panreac) and dimethyl formamide (DMF, chromatography grade, Fisher) were used as received.

Synthesis of PDMAPS macro-CTA

CPADB (0.08 g, 0.3 mmol), DMAPS (2.0 g, 0.7 mmol, target DP = 25) and AIBN (9.4 mg, 0.06 mmol, CTA/AIBN molar ratio = 5) were dissolved in 2,2,2-trifluoroethanol (2.5 mL) in a reaction tube. The reaction solution was stirred and degassed with nitrogen for 30 min before being placed in a pre-heated oil bath set at 70 °C. The polymerisation was allowed to proceed for 8 hours (Fig. 1a). An aliquot of the crude mixture was analysed by ^{1}H NMR spectroscopy to determine the monomer conversion (91%) (Fig. S1, ESI†). The product polymer was isolated by dialysis against pure water (regenerated cellulose membranes, 3500 g mol^{-1} molecular weight cut-off) and freeze-drying.

Synthesis of PDMAPS$_{24}$-*block*-(PBuMA$_{18.8}$-*stat*-PEHMA$_{6.3}$) diblock copolymer particles

pDMAPS$_{24}$ macro-CTA (0.39 g), *n*BuMA (0.15 g, 1.05 mmol, target DP = 18.8), EHMA (0.070 g, 0.35 mmol, target DP 6.3) and

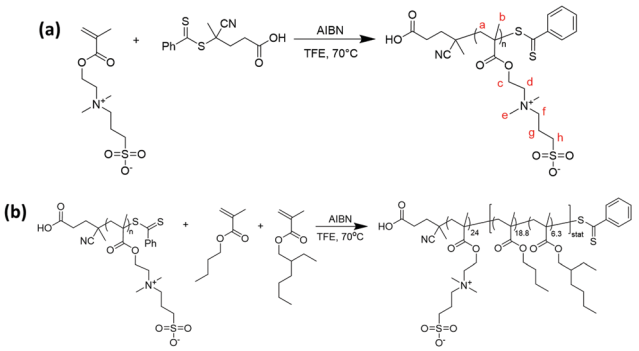

Fig. 1 (a) Synthesis of pDMAPS macro-CTA; (b) synthesis of pDMAPS$_{24}$-*block*-(pBuMA$_{18.8}$-*stat*-pEHMA$_{6.3}$) diblock copolymer.

AIBN (0.002 g, 0.013 mmol; macro CTA/AIBN molar ratio = 5) were dissolved in 2,2,2-trifluoroethanol (2.45 mL; 20% w/w) in a reaction tube. The reaction solution was stirred and degassed with nitrogen for 30 min before being placed in a pre-heated oil bath set at 70 °C. The polymerisation was allowed to proceed for 24 hours (Fig. 1b). Full conversion was confirmed by ^{1}H NMR spectroscopy by withdrawing a sample of the reaction mixture, evaporating the solvent, and dissolving the residue in trifluoroacetic acid-d (Fig. S2, ESI†). The diblock copolymer was purified and self-assembled into particles by dialysis against salt water (NaCl) and then pure water (regenerated cellulose membranes, 3500 g mol^{-1} molecular weight cut-off).

Synthesis of P(MMA-BA) particles

An aqueous dispersion of surfactant-free polymer particles was synthesized *via* emulsion polymerization of poly(methyl methacrylate/butyl acrylate) (MMA/BA: 1/1 by weight) and 1 weight% based on monomer of sodium styrene sulfonate (NaSS), as described elsewhere.[31] The glass transition temperature (T_g) was 19 °C,[32] and the solids content of the dispersion was 50 wt%.

Particle characterization

Dynamic light scattering (DLS) and zeta potential measurements were carried out in either a Malvern Zetasizer (PDMAPS particles) or a Litesizer 500 from Anton Paar (P(MMA-BA) particles). Samples for DLS analyses were prepared by diluting a fraction of the latex in distilled de-ionized (DDI) water (1 : 1000) to prevent multiple scattering. The analyses were carried out at 25 °C and a run consisted in 2 minutes of temperature equilibration followed by three size measurements per sample. An average of three is given as final value. Samples for zeta potential measurements were prepared by diluting the dispersions in DDI water and transferred to a folded capillary cell (DTS1060). The analyses were carried out at 25 °C and a run consisted in 2 minutes of temperature equilibration followed by three size measurements per sample. An average of three is given as final value.

Differential scanning calorimetry (DSC)

The glass transition temperature (T_g) of the zwitterionic latex was measured using a Q200 from TA Instruments. A droplet of the zwitterionic particle dispersion was dried and a sample

 This journal is © The Royal Society of Chemistry 2020

Open Access Article. Published on 17 August 2020. Downloaded on 12/4/2025 7:16:20 PM.
This article is licensed under a Creative Commons Attribution 3.0 Unported Licence.

of 5 mg was heated from −80 °C to 250 °C at 10 °C min^{-1} and kept at 250 °C for 1 min, then cooled down from 250 °C to −80 °C at 10 °C min^{-1} and kept at −80 °C for 1 min, then heated from −80 °C to 250 °C at 10 °C min^{-1}. The heat-flow curve from the second heating cycle was used to determine the T_g of the zwitterionic latex.

Preparation of colloidal films

The two particle dispersions were blended to obtain different zwitterionic particle volume fractions (in the dry film): $\phi_{zwitterionic}$ = 0.05, 0.18 and 0.35, corresponding to $\phi^{wet}_{zwitterionic}$ = 0.005, 0.016 and 0.033. 200 μL of the corresponding blend were cast on a square glass substrate (18 mm × 18 mm) which had been previously been washed with acetone, dried with compressed air and treated in a UV ozone cleaner (Ossila) for 10 minutes. Cast dispersions were dried at different evaporation rates: (i) fast evaporation, under a 250 W infra-red lamp (Intelec) at a distance of 10 cm; (ii) medium evaporation, at 21 ± 1 °C and 50 ± 10% RH; and (iii) slow evaporation, in a high humidity chamber at 21 ± 0.5 °C and ≥90% RH. Typical drying times were 7 min (fast evaporation), 3 h (medium evaporation), and 5 days (slow evaporation). The constant high humidity environment was created through heating deionized water at 50 °C on a hot plate in a semi-sealed Perspex box.

Atomic force microscopy (AFM)

The surface structure of the dried films was characterized using a NanoWizard® 3 from JPK Instruments in quantitative imaging (QI) mode. A silicon probe (NSG01 from NT-MDT) with nominal spring constant of 5 N m^{-1} was used. Topography images were analysed using JPK Data Processing software, and the surface roughness (R_a) was calculated by averaging values from three different areas in the sample. Adobe Photoshop was used to quantify the surface coverage of particles of different sizes. The area covered by a certain population of particles was selected using the lasso tool and the pixels in the area were counted. The surface coverage was quantified by dividing the number of pixels occupied by the selected particle population by the total number of pixels in the image. This process was averaged for at least 3 areas in each of two representative regions of the sample. The centre, in a radius of up to 5.5 mm from the centre of the glass coverslip, and the edge, at a range of 5.5–9.0 mm from the centre of the coverslip. Within each specific region and sample, the overall morphology was very similar and therefore one representative image was chosen when comparing AFM topography maps.

Water contact angle

The water contact angle of dried films was measured using a KRÜSS Drop Shape Analyzer DSA100. Five measurements were performed for each sample casting a 3 μl deionized water droplet each time and analysing the contact angle using Advance software.

Fourier-transform infrared (FTIR) spectroscopy – attenuated total reflection (ATR)

A Nicolet iN 10 MX Infrared Imaging Microscope from Thermo Scientific™, with a germanium crystal, was used to acquire FTIR-ATR spectra of the dried films. For each sample, a scan along a diagonal of the sample was obtained, measuring the FTIR-ATR spectra at 20 different positions across the film surface.

Scanning electron microscopy (SEM)

Cross-sections of dried films (coated with gold) were prepared by fracturing in liquid nitrogen and imaged using a Field Emission Scanning Electron Microscope (FEGSEM) from Zeiss (1530 VP) at an acceleration voltage of 5 kV.

Results and discussion

Particle characterization

Fig. 2 illustrates the size distribution in our colloidal system. The P(MMA-BA) particles have a fairly monodisperse size distribution centred around 250 nm. We will refer to these particles as medium particles from now onwards. However, the zwitterionic particles present two different particle populations, centred respectively at 28 nm and 396 nm, presenting broad size distributions. We will refer to these two populations as small particles and large particles, respectively. The zeta potential of P(MMA-BA) particles is −43 ± 1 mV, and they have a glass transition temperature T_g of 19 °C, as measured by DSC.[32] The zeta potential of the zwitterionic particles is −19.8 ± 0.5 mV, and the measured T_g of the butyl/hexyl methacrylate core is −8 °C as measured by DSC (see Fig. S3, ESI†). A T_g lower than room temperature indicates that these particles will be able to coalesce and interdiffuse after the dispersion is dried and film form.[9] Therefore, we do not expect to be able to visualize their morphology once dried in the film.

Structural characterization

Fig. 3 and 4 show AFM topography maps of the top surface of dried films close to the edge of the sample and at the centre for different volume fraction of zwitterionic particles ($\phi_{zwitterionic}$ = 0.05, 0.18 and 0.35) and formed at different evaporation rates;

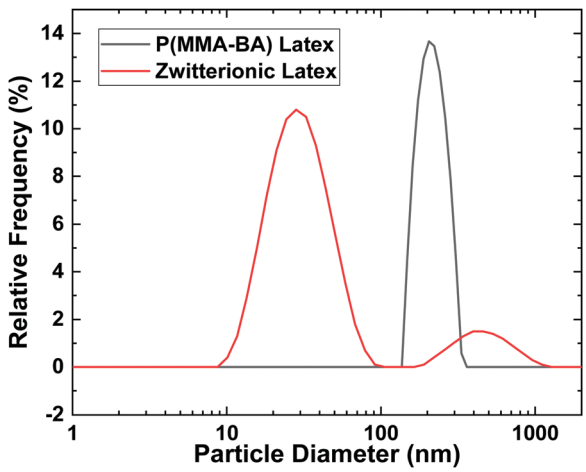

Fig. 2 Intensity weighted particle size distributions of P(MMA-BA) and zwitterionic latex particles.

Open Access Article. Published on 17 August 2020. Downloaded on 12/4/2025 7:16:20 PM.
This article is licensed under a Creative Commons Attribution 3.0 Unported Licence.

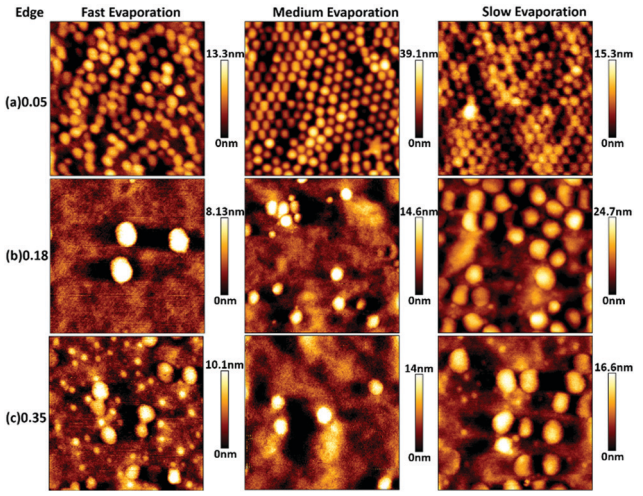

Fig. 3 AFM topography images (3 × 3 μm^2) of the edge region of P(MMA-BA) latex/zwitterionic latex films dried at fast (under infra-red lamp), medium (21 ± 1 °C and 50 ± 10% RH) and slow (> 90% RH) evaporation rate, for different zwitterionic latex volume fractions $\phi_{zwitterionic}$: (a) 0.05, (b) 0.18, and (c) 0.35.

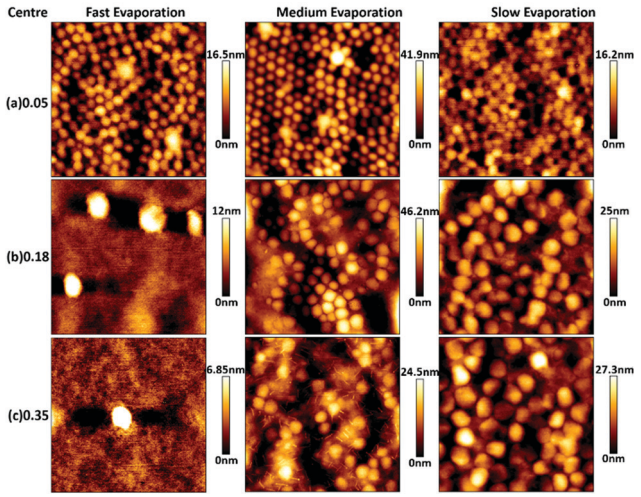

Fig. 4 AFM topography images (3 × 3 μm^2) of the centre region of P(MMA-BA) latex/zwitterionic latex films dried at fast (under infra-red lamp), medium (21 ± 1 °C and 50 ± 10% RH) and slow (>90%RH) evaporation rate, for different zwitterionic latex volume fractions $\phi_{zwitterionic}$: (a) 0.05, (b) 0.18, and (c) 0.35.

fast, medium, and slow. The first feature that can be observed is that the P(MMA-BA) particles present a clear spherical morphology and a fairly monodisperse particle size (Fig. 3a). However, the large zwitterionic particles are much more irregular in shape (Fig. 3b). The small zwitterionic particles coalesce fully during film formation due to their low glass transition temperature, and therefore their particle identity is not visible in the topography images. These clear differences in particle morphology enabled the use of image analysis to calculate the surface coverage θ of the three different particle size populations as a function of zwitterionic particles volume fraction and evaporation rate, as shown in Fig. 5.

For the lowest zwitterionic latex volume fraction ($\phi_{zwitterionic}$ = 0.05, Fig. 3a, 4a and 5), the top surface of the films is covered mainly by medium P(MMA-BA) particles and a few large zwitterionic particles. The evaporation rate used seems to affect mainly particle packing with a reduced degree of structural order at fast evaporation, and differences between sample centre and edge are not noticeable.

When the volume fraction of zwitterionic particles is increased to $\phi_{zwitterionic}$ = 0.18, the medium particles are mostly depleted from the top surface, which mainly shows small and large zwitterionic particles (Fig. 3b, 4b, and 5). This behaviour is observed for all evaporation rates and both at the edge and centre of the sample. As the evaporation rate increases, the number of large particles decreases to find only a few at the top surface when films are formed at fast evaporation rate. Very similar findings are observed when the volume fraction of zwitterionic particles is increased to $\phi_{zwitterionic}$ = 0.35. Medium particles are mostly depleted from the top film surface, which is dominated by small and large zwitterionic particles, as evidenced by the surface coverage graphs in Fig. 5. This shows how our particle system allows for a more robust system to ensure the presence of zwitterion groups at the surface.

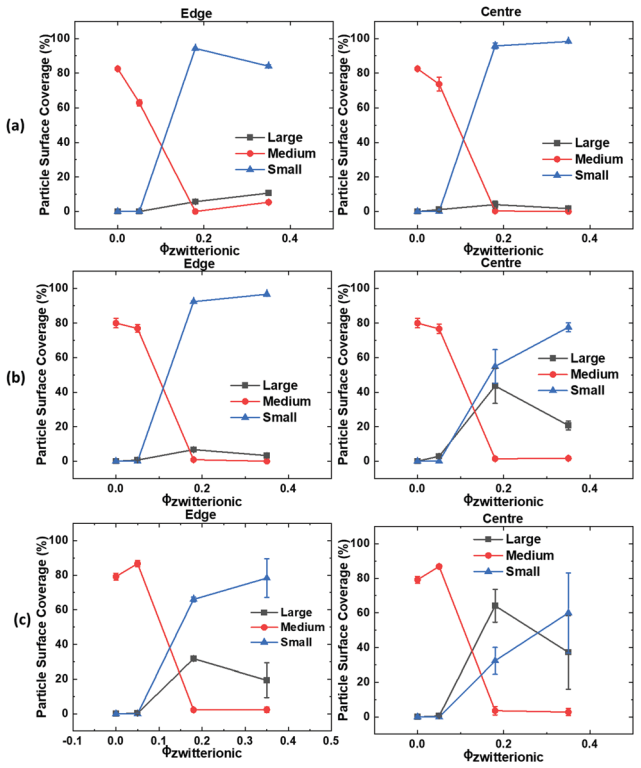

Fig. 5 Plots of surface coverage θ of small (28 nm in diameter), medium (250 nm) and large (396 nm) particle populations at the edge (left column) and centre (right column) *versus* zwitterionic latex volume fraction of films dried at fast (a), medium (b), and slow evaporation rate (c). Lines in between data points are guides for the eye.

The addition of large and small functional particles makes the size segregation process less sensitive to variations in evaporation rate than previously reported systems. We will discuss in a later section the possible assembly mechanisms involved.

 This journal is © The Royal Society of Chemistry 2020

Open Access Article. Published on 17 August 2020. Downloaded on 12/4/2025 7:16:20 PM.
This article is licensed under a Creative Commons Attribution 3.0 Unported Licence.

It is noteworthy to point out that the surface coverage by large particles at the centre of the film is generally larger than at the edge. This effect can be clearly seen by comparing the (b) and (c) rows of Fig. 3 and 4, and the corresponding surface coverage θ. In a drying colloidal dispersion, the water evaporation rate will be faster at the edges of the wet film than at the centre. This phenomenon results in a lateral flow of water from the centre to the edge. Such flow will affect nanoparticles in a stronger way, as they can be transported through closed packed arrays of larger particles.[33,34] As a result, the edge of the final dried film will present a larger content of small particles than its centre. If the evaporation rate is fast, then the nanoparticles are more likely to get trapped at the fast moving air/water interface reducing their lateral flow to the edge,[35] and the drying time will be significantly reduced, minimizing the time for the particles to move to the edges. These are the reasons why we do not observe large differences between the edge and centre of films dried at fast evaporation rate (Fig. 3b, c and 4b, c).

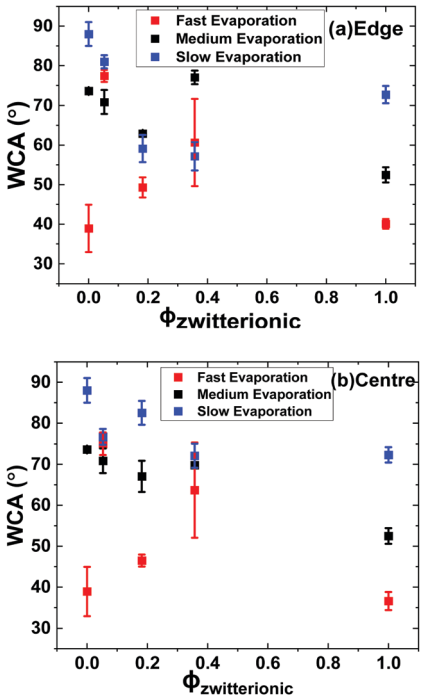

Fig. 6 Water contact angle of dried films at their edge (a) and centre (b) as a function of the zwitterionic latex volume fraction.

Fig. 6 shows the water contact angle (WCA) of the dried films *versus* the volume fraction of zwitterionic latex. The WCA of the control samples – *i.e.* pure P(MMA-BA) and pure zwitterionic particle films – seem to be correlated with the roughness of the surface (see Fig. S4, ESI†), with higher roughness resulting in higher WCA values. A further reduction in the contact angles for films dried at fast evaporation rate is expected because of the formation of microcracks on the surface as a result of a reduction in the time for the film to consolidate its structure, known as open time.[9,36] However, the WCA of the films cast from particle blends do not present a clear dependence with the surface roughness. This observation is probably explained by the combined effect of the surface roughness plus the surface composition, which varies depending on the evaporation rate and zwitterionic particle volume fraction used. Moreover, the presence of large and small zwitterionic particles also introduces a possible difference in the amount of zwitterion groups that might be present at the surface of each particle population, affecting the final wetting properties of the film.

In order to obtain a better understanding of the distribution of zwitterion groups not only at the very top surface but at the upper layer of films, FTIR-ATR scans of the samples were performed across diagonals of the samples. Fig. 7 shows representative FTIR-ATR spectra for control samples of P(MMA-BA) latex and pure zwitterionic latex films, as well as films with $\phi_{zwitterionic}$ = 0.18 and 0.35, dried at three different evaporation rates. The complete collection of spectra can be found in Fig. S5–S8 (ESI†). It can be observed that the main difference between the spectra of the P(MMA/BA) latex film and that of the pure zwitterionic latex film is the appearance of an absorbance peak at 1038 cm^{-1}, corresponding to the stretching of the S═O bond.[37] This group is also present in the P(MMA/BA) latex particles as part of the styrene sulfonate monomer, but as the NaSS content is only 1 wbm% its signal is weak. Therefore, we chose the peak at 1038 cm^{-1} as an indicator of the presence of zwitterion groups and normalized it to the absorbance of the C═O stretching peak at 1728 cm^{-1} to take into account differences in thickness between samples.

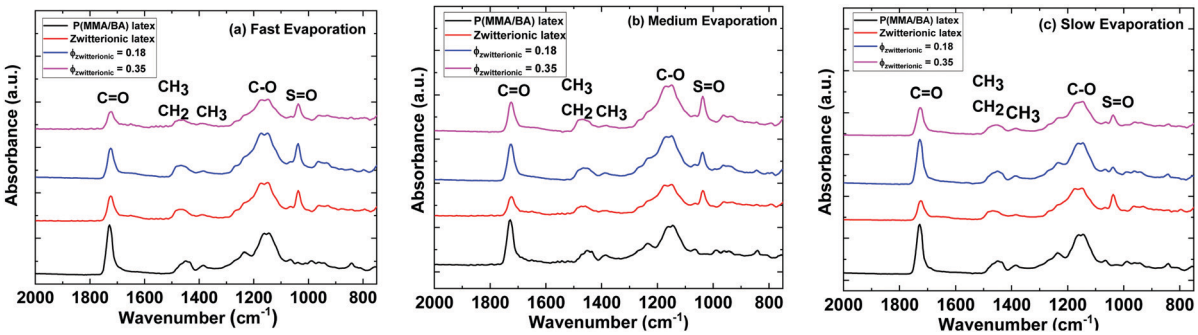

Fig. 7 Representative FTIR-ATR spectra of control P(MMA-BA) latex and zwitterionic latex films, as well as those films cast from blends containing $\phi_{zwitterionic}$ = 0.18 and 0.35. Evaporation rate is (a) fast, under an infrared lamp; (b) medium, at 21 ± 1 °C and 50 ± 10% RH; and (c) slow, >90% RH.

Open Access Article. Published on 17 August 2020. Downloaded on 12/4/2025 7:16:20 PM.
This article is licensed under a Creative Commons Attribution 3.0 Unported Licence.

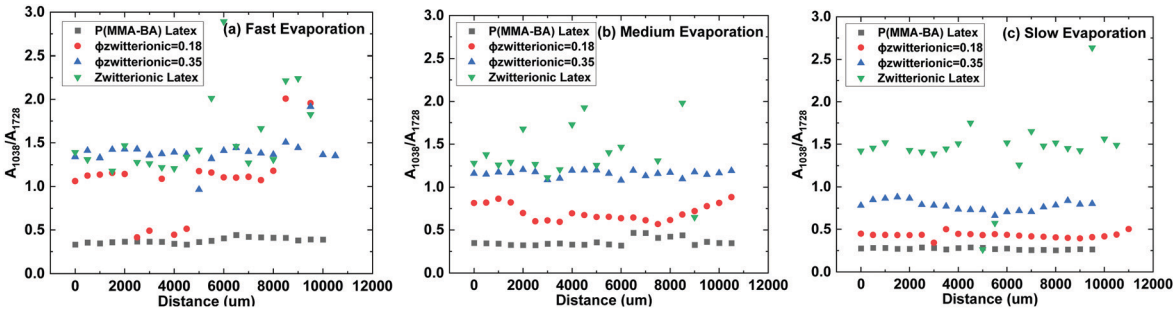

Fig. 8 Ratio between FTIR-ATR absorbances at 1038 cm^{-1} and 1728 cm^{-1} for dried latex films with different amount of zwitterionic particles at three different evaporation rates as a function of the distance along a diagonal of the sample.

The ratio A_{1038}/A_{1728} is presented in Fig. 8 as a function of the distance along a diagonal of the sample for the different film compositions and evaporation rates explored. Several initial observations can be deducted. First, the A_{1038}/A_{1728} ratio increases with increasing volume fraction of zwitterionic particles. Second, this ratio is larger the faster the films are evaporating. Such increase in absorbance ratio goes in line with the reasoning presented earlier of how a fast-moving air/water interface traps small zwitterionic nanoparticles and then they remain at the top film layer after drying. Third, the faster the evaporation rate the more data points fall out of trend. This is because of the increased roughness and the presence of cracks, which does not provide an optimal contact for an ATR measurement. For the pure zwitterionic latex film, which presents cracks visible to the naked eye, this is particularly notorious. In some cases, there is an increase in the absorbance ratio when reaching the edges (*e.g.* $\phi_{zwitterionic}$ = 0.18 in Fig. 8b and c) which might be related to the lateral flow of small particles to the edges at medium and slow evaporation rates. But generally, there does not seem to be a significant difference in the measured absorbance ratios between the edge and the centre of the samples.

We now compare the AFM and the FTIR-ATR results to obtain a more complete picture and discuss how complementary they are. Fig. 9a presents the absorbance ratio averaged over the FTIR-ATR scan, confirming quantitatively the increase in its value when either the evaporation rate or $\phi_{zwitterionic}$ increases. Fig. 9b presents the addition of the surface coverage θ by the small and large particles, *i.e.* the total surface coverage by zwitterionic particles using the numerical values from Fig. 5. Here, we also see an increase in the presence of zwitterionic particles at the surface when either evaporation rate or $\phi_{zwitterionic}$ increase, but a plateau of maximum surface coverage is reached at a lower value of $\phi_{zwitterionic}$. The combination of both graphs helps us to paint a more complete picture of the film architecture. AFM results provide information on the upper layer of the film, giving information about the particles that have been trapped at the air–water interface.

However, FTIR-ATR probes deeper into the sample. It is possible to calculate the penetration depth of the infrared light beam according to the equation:

$$d_p = \frac{\lambda}{2\pi n_c \sqrt{\sin^2\theta - \left(\frac{n_s}{n_c}\right)^2}}$$

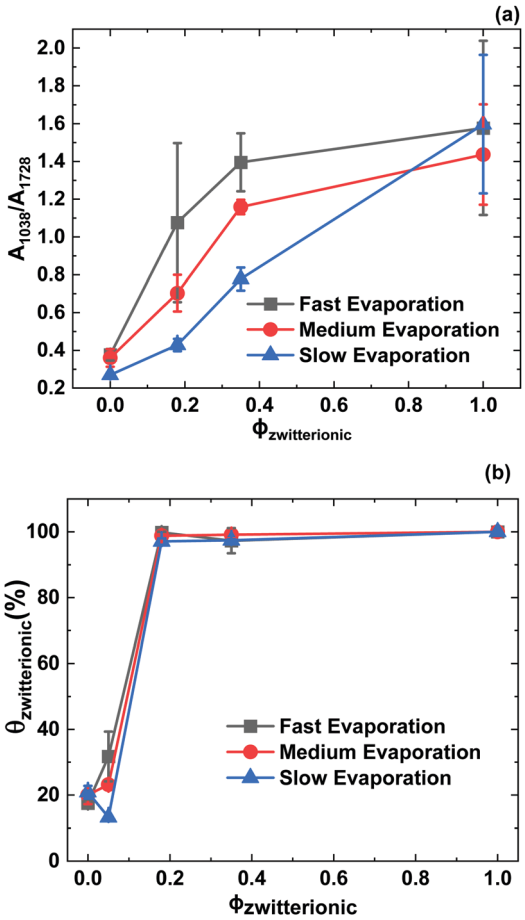

Fig. 9 (a) Ratio between FTIR-ATR absorbances at 1038 cm^{-1} and 1728 cm^{-1} averaged over a diagonal of the corresponding samples and (b) surface coverage by zwitterionic particles determined by AFM image analysis, as a function of the volume fraction of zwitterionic particles $\phi_{zwitterionic}$.

where d_p is the penetration depth of the beam, λ is the wavelength, n_c and n_s are the refractive indices of ATR crystal and sample, and θ is the incident angle.[38] For the wavelength range used in our experiments, the penetration depth is estimated to be between 0.107 and 1.07 μm which explains why FTIR-ATR results do not match precisely those obtained by AFM but provide complementary insights. The FTIR-ATR measurements show that even though the very top surface of the film is

Open Access Article. Published on 17 August 2020. Downloaded on 12/4/2025 7:16:20 PM.
This article is licensed under a Creative Commons Attribution 3.0 Unported Licence.

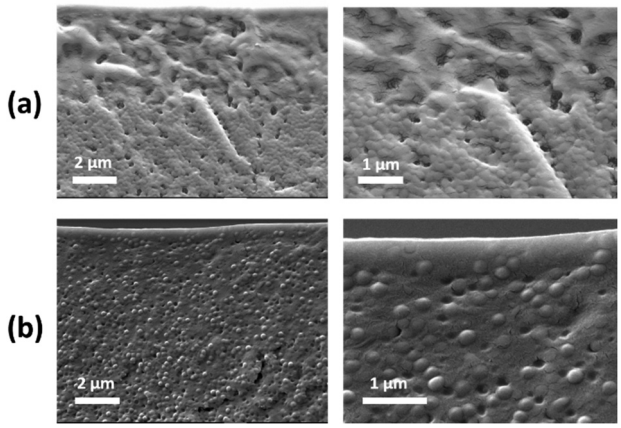

Fig. 10 Scanning electron microscopy cross-section imaging of P(MMA-BA) latex/zwitterionic latex films dried at (a) fast (under infra-red lamp) and (b) medium (21 ± 1 °C and 50 ± 10% RH) evaporation rates, for zwitterionic latex volume fraction $\phi_{zwitterionic}$ = 0.35.

covered by zwitterionic particles, its upper layer also contains non-zwitterionic particles. And the content of non-zwitterionic particles in such upper layer, which comprises between 0.1 and 1 μm, is reduced as we increase the evaporation rate. Therefore, using our polydisperse particle system we can ensure that the top surface is mostly covered by zwitterionic particles for a wide range of evaporation rates, as proven by AFM. But thanks to the FTIR-ATR measurements, we know that the content of zwitterion groups in the upper film layer can be maximised by increasing the evaporation rate. Such phenomena was observed in Brownian dynamics simulations by Howard *et al.*,[39] who reported a more uniform vertical distribution of the small particles in bimodal blends at slower evaporation rates. A faster moving air/water interface results in a larger gradient of particle concentration towards the substrate and a large driving force for the particle segregation.

In an attempt to visualize directly the distribution of zwitterionic particles throughout the film, cross-sections of the films with $\phi_{zwitterionic}$ = 0.35 were imaged using SEM. As can be appreciated in Fig. 10, films dried at fast evaporation rate (Fig. 10a) present a thicker and more distinct layer of small zwitterionic particles at the top than films dried at medium evaporation rate (Fig. 10b). It is important to have in mind a possible enhanced coalescence for the fast evaporation conditions, but the layer of closely packed medium particles underneath the top layer clearly contrasts with the much more homogeneous distribution in the medium evaporation case. These observations are in agreement with what was observed in the ATR-FTIR experiments (Fig. 9a), and serve as further proof of the enhanced size segregation that a faster evaporation rate provides.

Assembly mechanisms

In the first work on size segregation in drying polydisperse particle blends, Fortini *et al.* performed Brownian dynamics simulations to show how the final film composition varies with height, with the top of the film containing more small particles and the bottom containing more large particles.[12] This is the logical extension to polydisperse blends of the model that we developed earlier for stratification of drying bimodal blends.[11] In the films presented in this work, we observe medium particles are mostly depleted from the top surface but in some cases large particles make up for most of the surface coverage. It is important to remark that other possible configurations have been reported even in binary particle blends, such as large–small–large and small–large–small.[40] In their study, they attributed their observations to the use of significantly diluted dispersions (1.5% v/v), and the possibility of the formation of layers enriched in one of the particle populations at late stages of the drying process, as the model developed by Zhou[41] only considers partially dried films.

In our case we use more concentrated dispersions, but we cannot exclude the possibility of the formation of a layer of large particles during the drying process that gets trapped between the air/water interface and a layer enriched in small particles below. The formation of a monolayer of the larger particles at the top surface of drying particle blends has been observed in modelling studies on stratification of colloid and polymer-colloid systems.[14,39,42] It has been demonstrated throughout that in a binary mixture of hard spheres near a wall-which here is the air/water interface-, the large spheres are attracted to the wall because the small particles are depleting them from the inside of the dispersion. This results in an enrichment of the air–water interface with large particles and a depletion of small particles.[43] In the cited study and others, equilibrium conditions were assumed. That might be the reason why in our experiments we see a more predominant layer of large particles when we evaporate at slower evaporation rates, while only a few large particles are observed at the top at fast evaporation rate. It is also important to note that the presence of large particles at the top is heavily influenced by the inclusion of medium particles in the dispersion, as films made exclusively of zwitterionic particles show only small particles at the top (Fig. S9, ESI†). For a small number of large particles at the top surface, they do not have enough surface coverage to form clusters (Fig. 4b and c, left column). If they are present at the top surface in a large enough number, they can form a continuous layer at the top, as shown in Fig. 4c (slow evaporation). But the packing is not ideal because of the non-spherical shape of the particles and the uneven height of the film.

Underneath the layer of large particles, in some cases a layer mainly composed of small particles is observed with some medium particles partially sticking out (Fig. 3c). The reason why small particles are arranged around the medium particles instead of forming a flat layer on top is probably twofold. First, the number of small particles available in that region of the film might not be enough to form a uniform layer. Second, the zeta potential of the medium particles is much larger than that of the zwitterionic small particles. A smaller charge on the surface of the latter could result in a preference to arrange themselves around the medium particles rather than on top of them, as we have reported in blends of zinc oxide and latex particles with similar differences in zeta potential.[32]

Open Access Article. Published on 17 August 2020. Downloaded on 12/4/2025 7:16:20 PM.
This article is licensed under a Creative Commons Attribution 3.0 Unported Licence.

Conclusions

We have designed and synthesized a polydisperse colloidal system containing zwitterionic latex particles with a PDMAPS shell, with large (396 nm) and small (28 nm) particle diameters, and P(MMA/BA) latex particles, with medium particle diameters (250 nm). The purpose of such system was to harness size segregation during drying and maximize the presence of functional zwitterionic groups on the final film surface.

For volume fractions of the zwitterionic particles in the dry film of $\phi_{\text{zwitterionic}}$ = 0.18 and 0.35, AFM image analysis shows that the top surface is mostly covered by zwitterionic particles, both large and small, for all the evaporation rates explored. These correspond to drying times of 7 min (fast evaporation), 3 h (medium evaporation), and 5 days (slow evaporation). Achieving such surface coverage by the functional particles for a wide range of evaporation rates is a significant advance with respect to previous studies in bimodal particle blends where the drying speed would determine the elemental composition of the top of the film.

By making use of the deeper penetration of FTIR-ATR measurements, we obtained complementary insights on the composition of not only the very top surface but the upper layer (0.1–1 μm) of the film. Our results show that, although the AFM shows the top surface fully covered by zwitterionic particles, the content of zwitterionic particles of the upper layer does present a dependence with the evaporation rate. The faster the evaporation rate, the more zwitterionic particles that are contained within the upper film layer.

We hypothesized that in some cases a layer of large particles gets trapped at the air/water interface and remains there after jamming takes place, being found at the top of the film after drying. Underneath, small particles are arranged on top of medium particles, but they tend to accumulate around them rather than on top. We explained this observation based on differences in zeta potential, which make such situation more energetically favourable.

Our experiments show that polydisperse blends hold great potential to circumvent the sensitivity of the size segregation process in colloidal blends to evaporation rate. This is a key step to successfully apply such colloidal assembly processes in actual applications such as multicomponent antifouling coatings, where the evaporation rate cannot be tuned.

Conflicts of interest

There are no conflicts to declare.

Acknowledgements

The authors would like to thank Dr Anna Trybala for assistance with contact angle measurements and Dr Paul Roach for help and access to the FTIR-ATR instrument. We would like to thank Maialen Argaiz and Prof. Radmila Tomovska for providing the P(MMA-BA) latex samples.

Notes and references

1 A. Abdollahi, K. Sahandi-Zangabad and H. Roghani-Mamaqani, Rewritable Anticounterfeiting Polymer Inks Based on Functionalized Stimuli-Responsive Latex Particles Containing Spiropyran Photoswitches: Reversible Photopatterning and Security Marking, *ACS Appl. Mater. Interfaces*, 2018, **10**, 39279–39292.
2 E. Tekin, P. J. Smith and U. S. Schubert, Inkjet printing as a deposition and patterning tool for polymers and inorganic particles, *Soft Matter*, 2008, **4**, 703–713.
3 S. Deniz, M. Arca, M. S. Eroglu and E. Arca, Creating low energy paint surface using hollow sub-micron-latex particles, *Prog. Org. Coat.*, 2016, **98**, 14–17.
4 S. T. Eckersley and B. J. Helmer, Mechanistic considerations of particle size effects on film properties of hard/soft latex blends, *J. Coat. Technol.*, 1997, **69**, 97–107.
5 H. M. Van Der Kooij and J. Sprakel, Watching paint dry; more exciting than it seems, *Soft Matter*, 2015, **11**, 6353–6359.
6 I. Martín-Fabiani, *et al.*, Enhanced Water Barrier Properties of Surfactant-Free Polymer Films Obtained by MacroRAFT-Mediated Emulsion Polymerization, *ACS Appl. Mater. Interfaces*, 2018, **10**, 11221–11232.
7 T. N. Gevrek, K. Yu, J. N. Kizhakkedathu and A. Sanyal, Thiol-Reactive Polymers for Titanium Interfaces: Fabrication of Antimicrobial Coatings, *ACS Appl. Polym. Mater.*, 2019, **1**, 1308–1316.
8 R. Jovanović and M. A. Dubé, Emulsion-Based Pressure-Sensitive Adhesives: A Review, *J. Macromol. Sci., Polym. Rev.*, 2004, **44**, 1–51.
9 J. L. Keddie and A. F. Routh, *Fundamentals of Latex Film Formation*, Springer, Netherlands, 2010, DOI: 10.1007/978-90-481-2845-7.
10 S. Erkselius, L. Wadsö and O. J. Karlsson, Drying rate variations of latex dispersions due to salt induced skin formation, *J. Colloid Interface Sci.*, 2008, **317**, 83–95.
11 A. Fortini, *et al.*, Dynamic Stratification in Drying Films of Colloidal Mixtures, *Phys. Rev. Lett.*, 2016, **116**, 1–5.
12 A. Fortini and R. P. Sear, Stratification and Size Segregation of Ternary and Polydisperse Colloidal Suspensions during Drying, *Langmuir*, 2017, **33**, 4796–4805.
13 O. Cusola, *et al.*, Particulate Coatings via Evaporation-Induced Self-Assembly of Polydisperse Colloidal Lignin on Solid Interfaces, *Langmuir*, 2018, **34**, 5759–5771.
14 M. P. Howard, A. Nikoubashman and A. Z. Panagiotopoulos, Stratification Dynamics in Drying Colloidal Mixtures, *Langmuir*, 2017, **33**, 3685–3693.
15 I. Martín-Fabiani, *et al.*, pH-Switchable Stratification of Colloidal Coatings: Surfaces 'on Demand', *ACS Appl. Mater. Interfaces*, 2016, **8**, 34755–34761.
16 R. P. Sear, Stratification of mixtures in evaporating liquid films occurs only for a range of volume fractions of the smaller component, *J. Chem. Phys.*, 2018, **148**, 134909.
17 Y. Tang, G. S. Grest and S. Cheng, Control of Stratification in Drying Particle Suspensions via Temperature Gradients, *Langmuir*, 2019, **35**, 4296–4304.

 This journal is © The Royal Society of Chemistry 2020

Open Access Article. Published on 17 August 2020. Downloaded on 12/4/2025 7:16:20 PM.
This article is licensed under a Creative Commons Attribution 3.0 Unported Licence.

18 A. Statt, M. P. Howard and A. Z. Panagiotopoulos, Influence of hydrodynamic interactions on stratification in drying mixtures, *J. Chem. Phys.*, 2018, **149**, 024902.
19 Y. Tang, G. S. Grest and S. Cheng, Stratification of drying particle suspensions: Comparison of implicit and explicit solvent simulations, *J. Chem. Phys.*, 2019, **150**, 224901.
20 L. Zheng, H. S. Sundaram, Z. Wei, C. Li and Z. Yuan, Applications of zwitterionic polymers, *React. Funct. Polym.*, 2017, **118**, 51–61.
21 A. Laschewsky, Structures and synthesis of zwitterionic polymers, *Polymers*, 2014, **6**, 1544–1601.
22 J. M. Wates and A. James, Polybetaines as asphalt emulsifiers, *US Pat.*, US20020183401A1, 2003.
23 Y. Hu, *et al.*, The fabrication of superlow protein absorption zwitterionic coating by electrochemically mediated atom transfer radical polymerization and its application, *Acta Biomater.*, 2015, **13**, 142–149.
24 Y. Hu, *et al.*, Antifouling Zwitterionic Coating via Electrochemically Mediated Atom Transfer Radical Polymerization on Enzyme-Based Glucose Sensors for Long-Time Stability in 37 °C Serum, *Langmuir*, 2016, **32**, 11763–11770.
25 Y. F. Zhao, *et al.*, Versatile antifouling polyethersulfone filtration membranes modified via surface grafting of zwitterionic polymers from a reactive amphiphilic copolymer additive, *J. Colloid Interface Sci.*, 2015, **448**, 380–388.
26 N. Aldred, G. Li, Y. Gao, A. S. Clare and S. Jiang, Modulation of barnacle (Balanus amphitrite Darwin) cyprid settlement behavior by sulfobetaine and carboxybetaine methacrylate polymer coatings, *Biofouling*, 2010, **26**, 673–683.
27 M. Das, N. Sanson and E. Kumacheva, Zwitterionic poly(betaine-*N*-isopropylacrylamide) microgels: Properties and applications, *Chem. Mater.*, 2008, **20**, 7157–7163.
28 H. Willcock, *et al.*, One-pot synthesis of responsive sulfobetaine nanoparticles by RAFT polymerisation: The effect of branching on the UCST cloud point, *Polym. Chem.*, 2014, **5**, 1023–1030.
29 S. P. Bassett, *et al.*, One-pot synthesis of micron-sized polybetaine particles; Innovative use of supercritical carbon dioxide, *Polym. Chem.*, 2017, **8**, 4557–4564.
30 Z. Gui, *et al.*, Controllable disintegration of temperature-responsive self-assembled multilayer film based on polybetaine, *Colloids Surf., A*, 2011, **380**, 270–279.
31 S. Bilgin, R. Tomovska and J. M. Asua, Effect of ionic monomer concentration on latex and film properties for surfactant-free high solids content polymer dispersions, *Eur. Polym. J.*, 2017, **93**, 480–494.
32 Y. Dong, *et al.*, Zinc Oxide Superstructures in Colloidal Polymer Nanocomposite Films: Enhanced Antibacterial Activity through Slow Drying, *ACS Appl. Polym. Mater.*, 2020, **2**, 626–635.
33 D. J. Harris, J. C. Conrad and J. A. Lewis, Evaporative lithographic patterning of binary colloidal films, *Philos. Trans. R. Soc., A*, 2009, **367**, 5157–5165.
34 I. Martín-Fabiani, *et al.*, Design of Waterborne Nanoceria/Polymer Nanocomposite UV-Absorbing Coatings: Pickering versus Blended Particles, *ACS Appl. Nano Mater.*, 2018, **1**, 3956–3968.
35 Y. Li, Q. Yang, M. Li and Y. Song, Rate-dependent interface capture beyond the coffee-ring effect, *Sci. Rep.*, 2016, **6**, 1–8.
36 E. R. Dufresne, *et al.*, Flow and fracture in drying nanoparticle suspensions, *Phys. Rev. Lett.*, 2003, **91**, 1–4.
37 G. Socrates, *Infrared and Raman Characteristic Group Frequencies: Tables and Charts*, John Wiley & Sons, 2004, DOI: 10.1002/jrs.1238.
38 A. Götz, R. Nikzad-Langerodi, Y. Staedler, A. Bellaire and J. Saukel, Apparent penetration depth in attenuated total reflection Fourier-transform infrared (ATR-FTIR) spectroscopy of Allium cepa L. epidermis and cuticle, *Spectrochim. Acta, Part A*, 2020, **224**, 1–6.
39 M. P. Howard, A. Nikoubashman and A. Z. Panagiotopoulos, Stratification in Drying Polymer-Polymer and Colloid-Polymer Mixtures, *Langmuir*, 2017, **33**, 11390–11398.
40 W. Liu, A. J. Carr, K. G. Yager, A. F. Routh and S. R. Bhatia, Sandwich layering in binary nanoparticle films and effect of size ratio on stratification behavior, *J. Colloid Interface Sci.*, 2019, **538**, 209–217.
41 J. Zhou, Y. Jiang and M. Doi, Cross Interaction Drives Stratification in Drying Film of Binary Colloidal Mixtures, *Phys. Rev. Lett.*, 2017, **118**, 1–5.
42 W. Liu, J. Midya, M. Kappl, H. J. Butt and A. Nikoubashman, Segregation in Drying Binary Colloidal Droplets, *ACS Nano*, 2019, **13**, 4972–4979.
43 R. Roth and S. Dietrich, Binary hard-sphere fluids near a hard wall, *Phys. Rev. E: Stat. Phys., Plasmas, Fluids, Relat. Interdiscip. Top.*, 2000, **62**, 6926–6936.